Journal of Alloys and Compounds 787 (2019) 840–850

Contents lists available at ScienceDirect

Journal of Alloys and Compounds

journal homepage: http://www.elsevier.com/locate/jalcom

Short-range structural origins of serration events in metallic glasses

Mohit Kumar [a], Eric Nicholson [b], Donald W. Kirk [c], Steven J. Thorpe [b], Chandra Veer Singh [a, b, *]

[a] Department of Mechanical and Industrial Engineering, University of Toronto, 5 King's College Road, Toronto, Ontario M5S 3G8, Canada
[b] Department of Materials Science and Engineering, University of Toronto, 184 College Street, Suite 140, Toronto, Ontario M5S 3E4, Canada
[c] Department of Chemical Engineering and Applied Chemistry, University of Toronto, 200 College St., Toronto, Ontario M5S 3E5, Canada

ARTICLE INFO

Article history:
Received 24 September 2018
Received in revised form
31 January 2019
Accepted 4 February 2019
Available online 5 February 2019

Keywords:
Metallic glasses
Serrated flow
Short-range order
Molecular dynamics

ABSTRACT

Plastic deformation of metallic glasses under compression proceeds through sudden stress drops and accumulations known as serration or avalanche events. Experimental studies have suggested that this occurs by stick-slip behaviour of weak spots, while the atomistic structural origins underlying this phenomenon have remained unclear. In this study, we investigate deformation mechanisms underpinning serrated flow in Cu-Zr metallic glasses using molecular dynamics simulations. We show that this behaviour is essentially dictated by the short-range structural order as defined by the relative population of full icosahedra and geometrically unfavourable motifs (GUMs). The slip of atoms belonging to GUMs causes stress drops whose magnitude is directly correlated to the number of atoms involved in the slip. Continued loading leads to the breakdown of full icosahedra into GUMs, causing severe serration behaviour during the later stages of deformation. More severe and frequent stress drops are observed at higher temperatures and lower strain rates, indicating the thermally activated nature of this phenomenon. The compositions with lower Cu content show enhanced serrated flow, suggesting that ductility can be compositionally tuned. The statistical analysis of stress drops exhibits good agreement with previous experimental findings. Insights gained from this study will assist in designing new metallic glasses with superior ductility.

1. Introduction

The disordered structure of bulk metallic glasses (BMGs) provides them with a unique set of mechanical, chemical and physical properties due to which they have received a great deal of scientific and technological attention [1–12]. Metallic glasses are considered as brittle or quasi-brittle materials as they often fracture catastrophically under tensile loads due to highly localized, heterogeneous deformation via the formation of shear bands [4–7]. Increasing their ductility at room temperature has been an active area of research [13–17].

Shear transformation zones (STZs) are the carriers of plastic deformation at the atomic level in metallic glasses [18] and shear localization evolves from STZs into thin bands of strain-weakened material. The propagation of one of these shear bands eventually penetrates the entire sample leading to failure. Recently, Pan et al. have shown that the control of shear bands can lead to extreme rejuvenation and softening in a zirconium based bulk metallic glass [19]. In a specific range of temperature and applied strain rate [20–23], shear bands show stick–slip behaviour with alternating phases of stress drops and accumulations. One such drop and burst cycle is known as a serration event.

The inhomogeneous serrated plastic flow uncovered in one of the first experimental studies indicated the modification of atomic structure during straining [24], which was subsequently corroborated in various studies [25–29]. Liao et al. have found the volume of the STZs to increase during serrated flow in nanoindentation [30]. Antonaglia et al. [31,32] have concluded that BMGs deform in compression via slip avalanches of coupled weak spots present in the glass matrix. They have reported that serrations exhibit a scaling behaviour, i.e., a cumulative size distribution which follows a power law. Thurnheer et al. [23,33] investigated the role of composition in a ternary Cu-Zr-Al alloy on shear band dynamics, finding that the activation barrier for shear-band propagation is correlated with the ratio of strong Cu-Zr to weaker Cu–Cu bonds, and significantly dependent on strain rate. The compression tests

* Corresponding author. Department of Mechanical and Industrial Engineering, University of Toronto, 5 King's College Road, Toronto, Ontario M5S 3G8, Canada.
E-mail address: chandraveer.singh@utoronto.ca (C.V. Singh).

https://doi.org/10.1016/j.jallcom.2019.02.037
0925-8388/

were carried out on pre-notched samples to artificially control the dominant deformation behaviour. Li et al. [34] have reported a linear relation between the logarithm of strain rates and mean stress drops in experimental work on Zr-based BMGs.

Serration behaviour enhances plasticity of a BMG sample and fundamental understanding of the underlying mechanisms is required to design new BMG materials with superior ductility. Despite the overwhelming interest and extensive experimental investigation, a comprehensive treatment of the atomistic mechanism of serration events and effect of various parameters on serration behaviour from a simulation perspective is yet to be undertaken. Feng et al. suggest a correlation between deformation and local structural order [35]. Tang et al. argue for the participation of local fivefold symmetric sites in stress overshoots [36]. Da et al. have shown the development of free volumes in Zr_2Cu [37] which may allow for local atomic rearrangement. The underlying mechanisms behind serration events are not fully resolved. For instance, it is not yet clear which atoms participate in plastic slips that lead to stress drops. Also, the details of atomic rearrangements needed to cause serration events have not been investigated so far. Furthermore, what parameters control the size of the slip avalanche and magnitude of the stress drop and how? Such questions remain and need to be addressed.

Here, we use molecular dynamics (MD) simulations to uncover the relationship between serration events on the stress-strain curve and their corresponding atomic level structural changes. The uniaxial tensile loading employed in the simulations is uniform and does not generate any artificial defect site(s) for nucleation of shear localization which could result in homogeneous flow. The simulated metallic glass (MG) structure exhibits symmetrical response to compressive and tensile loading, plastically yielding by serrated flow in tension in contrast to experimentally observed brittle failure, suggesting a separate mechanism is active on longer time scales than are accessible to these MD simulations that results in brittle fracture under tension. A relatively slow MD strain rate of 10^7 s^{-1} was used to deform the samples (Fig. 1) and investigate inhomogeneous deformation. Simulations were carried out over a range of strain rates, temperatures, and compositions of Cu-Zr alloy and a detailed analysis is presented on the effect of these parameters on serration behaviour. The applicability of relevant experimentally established empirical models is also tested.

2. Experimental details

MD simulations were carried out using the LAMMPS package [38]. Many-body embedded atom method (EAM) interatomic potentials developed by Mendelev [39] for Cu-Zr were used to describe atomic interactions. MG samples with Cu_xZr_{100-x} ($x = 35$, 50, 56 and 64) were generated by first populating a box of ~10,000 atoms with Cu and Zr atoms in the required atomic fractions according to a B2 structured supercell. The simulation box was first relaxed at 300 K with 3-D periodic boundaries under a zero pressure barostatic condition and then heated from 300 K to 2100 K over a duration of 1 ns. It was followed by a relaxation stage for 2 ns to ensure that the high-temperature liquid melt is properly equilibrated. Next, the samples were rapidly quenched at a cooling rate of 100 K ns^{-1} to a final temperature of 25 K through a series of quench and hold stages. The temperature was brought down in steps of 25 K; cooled for 0.1 ns and then relaxed for 0.15 ns at that temperature. NPT Nose-Hoover temperature and pressure controls with 1 fs time-step were used to enforce zero pressure isobaric conditions throughout the quenching process. The quenched samples were further relaxed in NVT ensemble for 0.2 ns and atomic positions, velocities, and energies were sampled for particular temperatures.

The data collected from MD simulations were post-processed to obtain various structural, thermodynamic and kinetic properties, the details of which are provided in our previous report [40]. The calculated properties such as radial distribution function, structure factor, melting point, glass transition temperature, etc., were compared to the existing experimental and simulation data from literature for establishing the physical and chemical validity of the sample under study, as further discussed in the results section.

For mechanical testing simulations, larger samples with

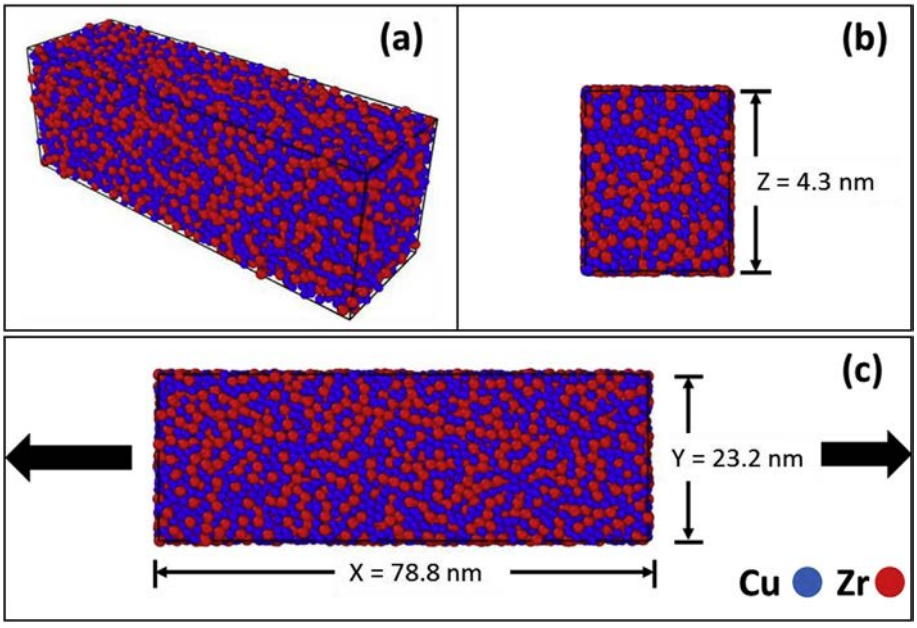

Fig. 1. Typical atomistic configuration of a simulated sample. (a) Atomic structure of $Cu_{64}Zr_{36}$ MG sample showing dense atomic packing of ~500,000 atoms. (b) Left hand side view of a typical sample configuration used for mechanical testing simulations depicting system size along periodic Z direction. (c) Front view of a typical sample depicting sample size along periodic X and shrink-wrapped Y direction. Uniaxial tensile loading was carried out, as depicted by arrows, along the X direction to deform the samples.

dimensions of $78.8 \times 23.2 \times 4.3\,nm^3$ and containing ~500,000 atoms were prepared with the same cooling rate and relaxation times as for the smaller cell. MG samples were loaded in uniaxial tensile deformation mode, with a constant strain rate of 1.0×10^7/s applied along the X-direction. Fig. 1 shows the 3-dimensional left-hand side and front view of a typical sample configuration used for mechanical testing simulations with arrows depicting the uniaxial loading in X-direction. While the X and Z-directions were imposed with periodic boundary conditions, the Y-direction was imposed with a free boundary condition to allow for shear offset during deformation.

In experimental BMG mechanics, deformation is accommodated by shear bands [41] appearing on micron sized scales which are difficult to replicate in MD. Some examples of these larger length scale effects are interactions between multiple shear bands will affect the distribution of stress drops in serrated flow [42] and chemical heterogeneities can stimulate shear band formation and intersection resulting in plasticity [28]. Plastic shearing of BMGs may produce local internal stresses in the opposing direction which may reach 90% of the magnitude of the globally applied stress [43]. In microscopic terms this may be thought of in terms of an analogue to classical dislocations in metals [44]. In further work these long-range stresses may be accounted for by applying appropriate boundary conditions to the simulation cell, but in these MD simulations we have restricted our focus to a uniaxial strain which will necessarily ignore the complex long-range stress field effects of the dislocation-like deformation behaviour. Still, the illustration of atomistic rearrangement in MGs simulated here provides insight into the lowest level of the hierarchy of processes occurring in the macroscopic deformation of BMGs.

3. Results and discussion

In order to verify the structure of MG samples prepared by MD, the structure factor was calculated for various compositions and compared with available experimentally obtained structure factors. Fig. 2(a) depicts the structure factor calculated from the data collected through simulations for four different Cu-Zr compositions. Clearly, the computed structure factors exhibit remarkable agreement with the experimental values obtained from previous XRD observations [45], including the shape, magnitude and the peak locations. Fig. 2(b) shows the evolution of structure factor at different temperatures during quenching of a $Cu_{64}Zr_{36}$ sample. The location of the first peak, q_1, remains fairly constant up to the glass transition temperature T_g ~760 K whereas the height of first peak, $S(q_1)$, decreases with increasing temperature, as expected. After T_g, at the next temperature investigated (1300 K), there is a significant decrease in the location (q_1) as well as height $S(q_1)$ of the first peak. The liquid state of the sample above T_g is reflected by this diffuse shape of the curve.

3.1. Overall stress-strain response and structural origin of serration events

Fig. 3(a) represents the stress-strain curve of the $Cu_{64}Zr_{36}$ MG sample loaded in uniaxial tension along X-direction. As expected the data is linear in the initial elastic deformation regime up to ~3.5% strain, beyond which the system enters a regime where plastic deformation proceeded with repeating cycles of stress drop and accumulation (serration events).

Serration events were observed to occur in both tension and compression (Fig. 4), and only small shear bands are observed to form (Fig. 5) suggesting that the dominant shear bands that lead to failure [41] are formed in a process beyond the time and length scale limitations of MD. Still, the inspection of atomic configurations of the small shear band serration events present in these simulations illustrate a plausible mechanism for the evolution of local structure in MGs under uniaxial loading.

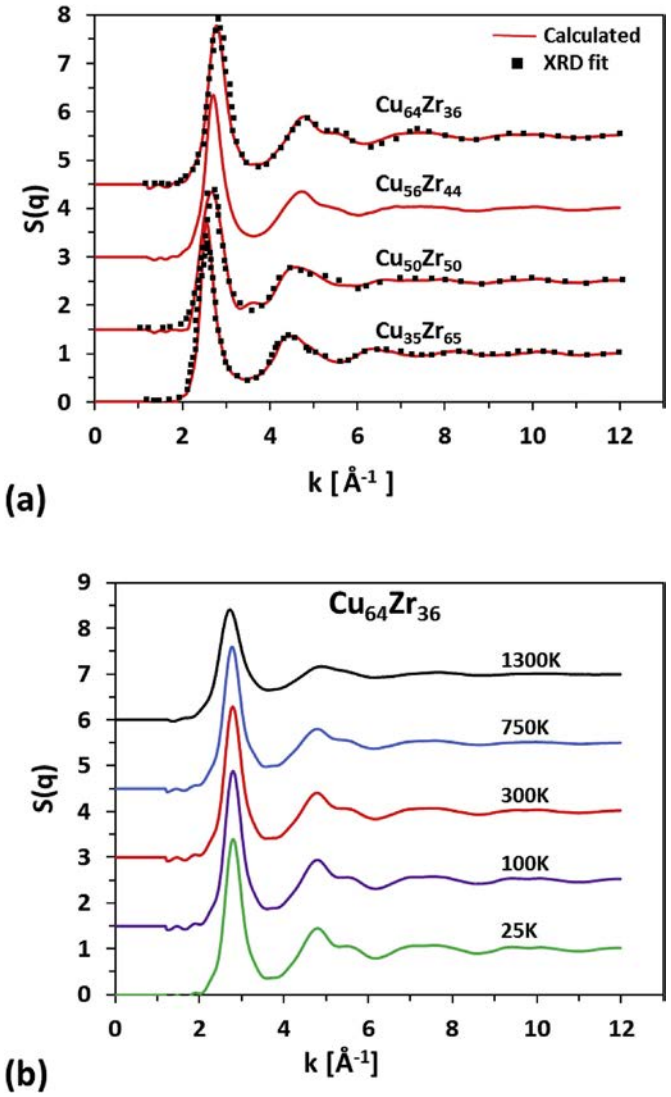

Fig. 2. The effects of composition and temperature on local order. (a) Calculated structure factor for various samples of Cu-Zr compositions at 300 K. (b) Structure factor evolution during quenching for a simulated $Cu_{64}Zr_{36}$ MG specimen plotted at various temperatures. The structure factors of the simulated Cu-Zr MGs exhibit excellent agreement with structure factors obtained experimentally via XRD [45].

In order to uncover the processes happening at the atomic level corresponding to serration events on stress-strain curves, we used atomistic visualization and analysis packages AtomEye [46] and Ovito [47]. The local atomic shear strain, η^{Mises} [46] was calculated to quantify and monitor the deformation process. The local shear invariant of an atom, a measure of its atomistic local strain between a reference state and present state, is given by

$$\eta^{Mises} = \sqrt{\eta_{yz}^2 + \eta_{xz}^2 + \eta_{xy}^2 + \frac{\left(\eta_{yy} - \eta_{zz}\right)^2 + \left(\eta_{zz} - \eta_{xx}\right)^2 + \left(\eta_{xx} - \eta_{yy}\right)^2}{6}} \quad (1)$$

η^{Mises} is a widely used metric for inhomogeneous deformation in atomistic simulations [48,49].

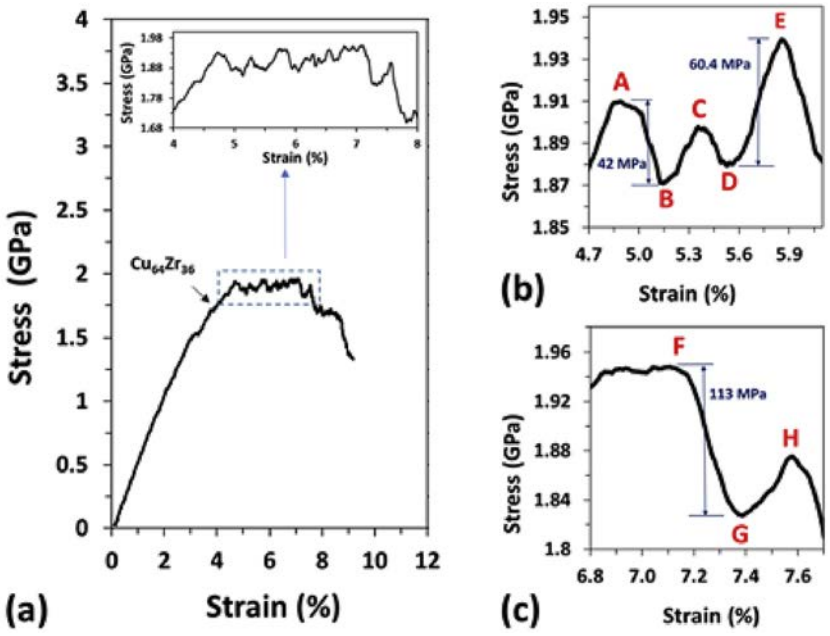

Fig. 3. Representative stress-strain response. (a) Stress-strain response of $Cu_{64}Zr_{36}$ MG sample at 10^7/s strain rate and 300 K. The stress-strain curve of MG sample contains repeated cycles of stress drop and accumulation. (b)–(c) Stress drop and accumulation events analysed in greater detail (see e.g. Figs. 5 and 6).

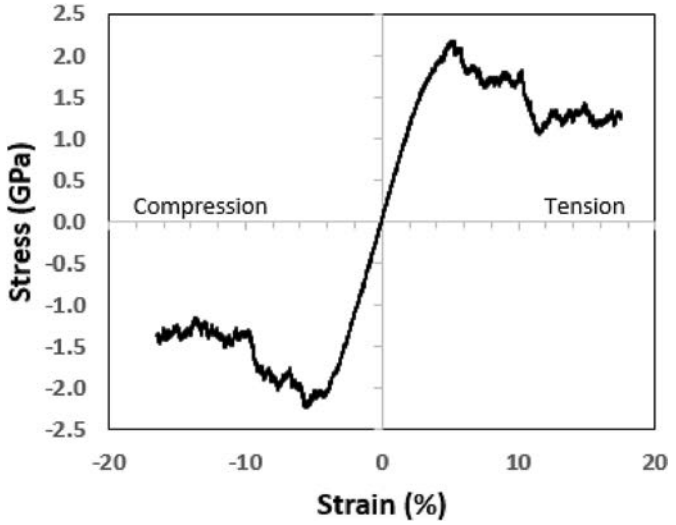

Fig. 4. Stress-strain response of a $Cu_{64}Zr_{36}$ cell in separate uniaxial tension and compression loading simulations.

During the initial stages of deformation, the distribution of η^{Mises} was uniform throughout the sample with a value close to zero, indicating that there is little inelastic movement of atoms and the system is in the elastic regime. When the system entered the inelastic regime (ε ~3.5%), some spots with η^{Mises} relatively greater than the bulk sample started to appear at random locations in the sample. These spots are the locations of STZs. As the deformation proceeded, more and more STZs started appearing in groups or clusters (coalesced STZs) in the sample. This coalescing of STZs with higher η^{Mises} values indicates grouped slipping of these atoms/clusters.

By comparing the simulation time-step of coalescing STZs with the corresponding point on the stress-strain curve, we determined that each grouped slipping of atoms/clusters corresponded directly to a stress-drop event. The next task was to distinguish these groups of atoms from those in the bulk sample and to characterize said groups. For further investigation, we focussed our analysis on randomly picked representative serration events – stress drop event AB, stress accumulation event DE and a stress drop event of relatively greater magnitude, FG, as shown in Fig. 3(b)–(c) with their corresponding stress change magnitudes. Fig. 5 denotes the atomistic configuration snapshots of the sample corresponding to points A, B, C, D, E, F, G and H. Atoms are colored according to their least square local atomic strain (η_i^{Mises}).

As the stress dropped from point A to B, STZs coalesced into bands of shear localization along with the generation of new STZs as seen in the corresponding snapshot B. When stress accumulated from B to C, these bands became diffuse and no new STZs appeared in the sample. Again, when the stress dropped from C to D, coalescing of STZs into shear bands can be seen. With the subsequent increase in stress from D to E, these shear bands are arrested and diffused. Similarly, during the stress drop event from F to G, which has a greater magnitude of stress drop compared with AB, more STZs appeared and coalesced into bands. In view of these atomistic configuration snapshots, stress drop events AB, CD and FG were found to be associated with formation of shear bands evolving from coalesced STZs. In contrast, stress gain events were associated with diffusing shear bands and arrest of any inelastic atomic movements. This corroborates the claim that stress gain events are elastic reloading in nature. Also, the magnitude of η_i^{Mises} has increased indicating that a larger inelastic atomic movement had taken place. Again, as the stress increased up to point H, these bands diffuse and no new STZ formation or increase in η_i^{Mises} was observed.

From the observations above, it can be noted that the stress drop events occurred due to coupled slipping of several weak spots, or coalescing of several STZs resulting in the nucleation of a shear band. Such shear bands have been termed as embryonic shear bands [48]. These embryonic shear bands propagate leading to a stress drop event, but are eventually arrested. In bulk MG samples, usually one of the embryonic shear band develops into a major shear band, which eventually runs across the sample localizing all

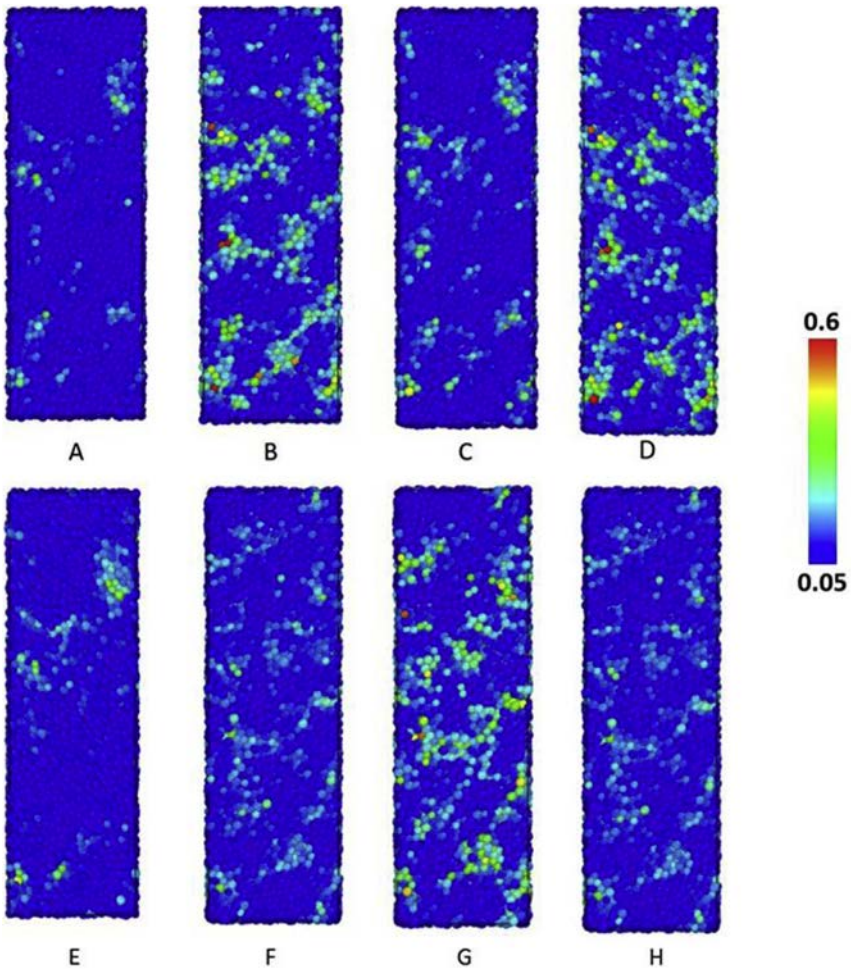

Fig. 5. Atomic configuration snapshots corresponding to points A to H (Fig. 3(b)-(c)). At instant A & F, STZs can be seen popping throughout the system, however these atomic groups still have lower η_i^{Mises}. After the stress drop, at instants B & G, STZs coalescing into shear bands can be seen. At instants C & H, when the stress is re-accumulated, the shear bands become diffuse. This shows that higher inelastic movement of atoms (slip) occurs during a stress drop event, whereas there is little inelastic movement of atoms during stress accumulation events. Atoms are colored according to their atomic local shear strain (η_i^{Mises}).

plastic deformation into itself, leading to fracture. In contrast, a stress accumulation event shows negligible or very small plastic deformation (lower values of η^{Mises}), indicative of an elastic reloading of the sample. In some studies, it was found that the slopes of stress accumulation events are parallel to each other and are equal in magnitude to the Young's modulus [15], further supporting the assertion of elastic reloading.

To further probe the mechanism of atomic transitions in individual serration events, we calculated η_i^{Mises} between atomic states at the start and end of stress-change events. The atomic local shear invariant, η_i^{Mises}, is a measure of plastic deformation at the atomic level for a specified atomic configuration with respect to a reference configuration. To quantify the local atomic movements in each serration event, we calculated η_i^{Mises} between the atomic configurations before and after a serration event. For example, for a stress-drop event AB, η_i^{Mises} was calculated by taking the atomic state at B as the current configuration and the atomic state at A as its reference configuration. We note the maximum η_i^{Mises} and the number of atoms with η_i^{Mises} exceeding 0.15. Five stress accumulation events and seven stress drop events were analysed in this way and are summarized in Table 1.

The atomic configurations during stress accumulation events are characterized by an η_i^{Mises} not exceeding 0.15. A correlation between the stress drop magnitude and number of atoms with $\eta_i^{Mises} > 0.15$ can be seen for stress drop events, where the events with greater stress drop magnitudes employ a larger number of atoms to accommodate plastic slip. The summary of η_i^{Mises} calculation for the three serration events under closer analysis (i.e. AB, DE and FG) is presented in Table 2.

The distribution of η_i^{Mises} for the three events is presented in Fig. 6(a). The average η_i^{Mises} is lowest for the stress accumulation event DE (coloured black) with maximum $\eta_i^{Mises} = 0.15$; whereas for stress drop events AB(blue) and FG(red) the average η_i^{Mises} is higher and skews higher, with maximum η_i^{Mises} of 0.25 and 0.35, respectively. This diffuse shape indicates that more local inhomogeneous atomic movements/slips have taken place. Event FG has a larger stress drop (113 MPa) compared to that of AB (42 MPa) and the maximum value of η^{Mises} for the atoms in event FG is greater than the atoms in AB. More interestingly, the number of atoms involved in plastic slipping is also greater for FG than AB. Here, the number of atoms involved represents all atoms which have $\eta^{\text{Mises}} >$ 0.15. This signifies that the magnitude of a stress drop event directly corresponds to the number of atoms involved in the slip avalanche. Furthermore, from the atomic configuration snapshots, Fig. 6(b),

Table 1
Summary of calculation of η_i^{Mises} for analysed serration events.

	Stress Change Magnitude (MPa)	Maximum η_i^{Mises}	Number of atoms with $\eta_i^{Mises} > 0.15$
Stress Accumulation Events	36	0.09	0
	43	0.11	0
	60.4	0.14	0
	81	0.12	0
	94	0.15	0
Stress Drop Events	23	0.18	988
	37	0.21	1102
	42	0.25	1558
	74	0.26	2204
	98	0.33	3306
	113	0.35	4180
	131	0.38	5282

Table 2
Summary of analysis of events AB, DE and FG.

Serration Event	AB	DE	FG
Stress Change Magnitude (MPa)	42	60.4	113
Max η_i^{Mises}	0.25	0.14	0.35
Number of atoms involved in the slip	1558	0	4180

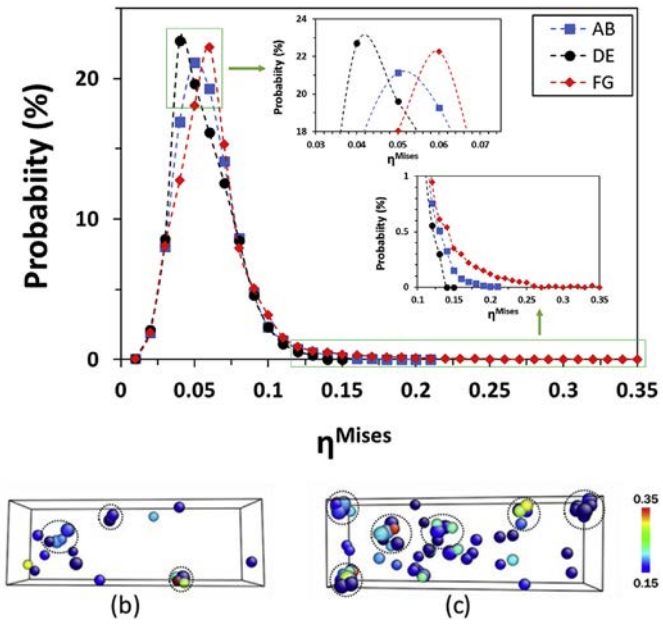

Fig. 6. Von Mises stress distributions. (a) The atomic distribution of η_i^{Mises} calculated between instants prior to and after a stress changes event. (b)–(c) Atomic configuration snapshots of (b) event AB and (c) event FG showing atoms with $\eta_i^{Mises} > 0.15$. Atoms are present in groups/clusters (circled).

showing the atoms above $\eta^{Mises} > 0.15$ for stress-drop event AB and FG, it is evident that atoms involved in the slips are present in groups/clusters (circled). Again, event FG has more such groups than AB, since it is an event of larger stress drop and involves more atoms in the slip avalanche.

These atoms/groups of atoms were then mapped to their corresponding Voronoi polyhedron type. The Voronoi tessellation method is widely used to describe short-range order and packing of atoms in amorphous structures in terms of atomic coordination number and types of coordination polyhedra [49]. The nearest neighbour geometry is decomposed into a polyhedron centred around each atomic site. The Voro++ package [50] was used to perform Voronoi tessellations. System snapshots are taken every 256 time-steps over a sampling duration of 32 ps allowing for improved cluster statistics.

Fig. 7 represents the fraction (%) of six major Cu-centred Voronoi polyhedra and geometrically unfavoured motifs (GUMs) describing the short-range order of a $Cu_{64}Zr_{36}$ MG sample. GUMs are essentially low population polyhedra which have unfavourable coordination numbers, lower symmetry, and higher configurational entropy [51]. These are clusters of atoms that are more flexible and amenable to rearrangement upon the application of stress. Such polyhedra readily undergo shear transitions.

The one to one mapping of some of the groups of atoms to their corresponding Voronoi polyhedra revealed that at instant A, i.e. just before the stress drop, these atoms were present in polyhedra with Voronoi index Cu <0,3,6,2>, Zr <0,3,6,8> and Cu <0,4,6,3>. After the slip avalanche, i.e. at instant B, these polyhedra have evolved into Cu <1,2,5,3>, Zr <3,7,6,1> and Cu <0,2,6,5>, respectively. Similarly, for event FG, at instant F, some of the groups of atoms were present in polyhedra with Voronoi index Cu <0,4,4,3>, Cu <0,0,12,2>, Cu <0,1,10,3>, Zr <0,2,8,8> and Zr <2,9,4,1> and after the slip avalanche, i.e. at instant E, these polyhedra have evolved into Cu <2,2,4,3>, Cu <0,1,10,4>, Cu <0,3,6,5>, Zr <0,1,10,7> and Zr <0,4,4,8>, respectively.

It is worth noting that most of the Voronoi polyhedra that are accommodating the inelastic movement in the slip avalanche and are readily evolving belong to the category of geometrically unfavourable motifs (GUMs), which represent the 'liquid-like' structural units in the amorphous structure. In short, such polyhedra easily undergo shear transformations (STs) and thus make up the 'weak spots' in the material matrix. Hence, it can be deduced that stress-drop events are due to coupled slipping of several geometrically unfavourable polyhedra acting as weak spots in the sample, and the greater the number of such weak spots involved in the slip, the greater the magnitude of the stress drop. The plastic deformation proceeded by nucleation, propagation and arrest of these slip avalanches leading to serrated flow.

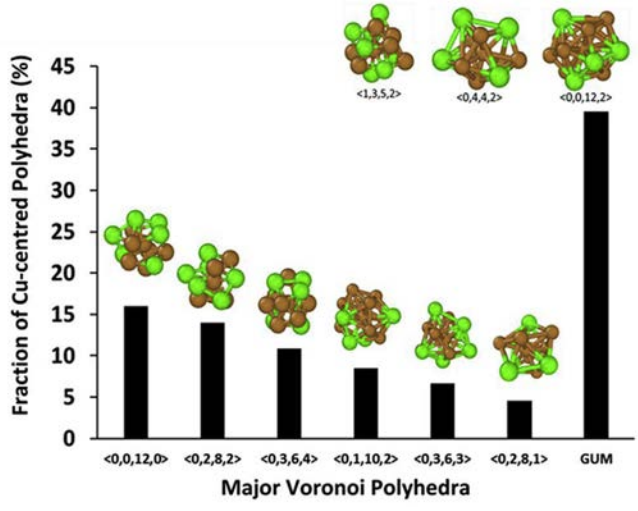

Fig. 7. Fraction of six major Cu-centred Voronoi polyhedra and geometrically unfavoured motifs (GUMs) describing the short-range order of the $Cu_{64}Zr_{36}$ MG sample. Atomic configuration of each Voronoi polyhedron type is as shown with bigger atoms (green) representing Zr and smaller atoms (bronze) representing Cu respectively. Bonds are drawn to help better visualization of nearest neighbour atoms and cluster shapes. (For interpretation of the references to color in this figure legend, the reader is referred to the Web version of this article.)

3.2. Evolution of serration behaviour with applied strain

It has been reported in experimental studies [15,52] that the magnitude of stress drops is increased with an increase in applied strain. To understand the fundamental atomistic mechanism responsible for this behaviour, we performed a statistical analysis of stress drops with respect to overall sample strain. The results are given in Fig. 8(a). For this analysis, only stress changes above 15 MPa (at least 1.5 meV/atom) were considered to exclude average ensemble effects.

From Fig. 8(a), it is clear that both the number of serration events and the magnitude of the average stress change, ($\Delta\overline{\sigma}$), followed an increasing trend with an increase in applied strain magnitude. This implies that during the late stages of deformation more serration events were taking place and with larger magnitudes, indicating that shear transformations were more localized. This phenomenon can be explained with the help of Fig. 8(b), which depicts the evolution of major polyhedra in the bulk sample with overall sample strain. As the deformation proceeded, the frequency of all the polyhedra types remained almost constant up to ~3.5% strain, after which the frequency of the full icosahedral (FI) <0,0,12,0> motif declined and the frequency of GUMs started rising, whereas there is no significant change in the frequencies of all other major polyhedra.

It is well known that the FI motifs are the most stable geometrical units in metallic glasses and are most resistant to shear transformations. They form the structural backbone of the amorphous sample and all other motifs are interconnected in an FI matrix. Thus, the FI network needs to break down in order to accommodate any plastic deformation [53]. FI motifs started breaking down into GUMs as the deformation proceeded in the plastic regime. The increase in the GUMs population resulted in an increase of nucleation sites for STZs. Since the coalescing and coupled slipping of STZs resulted in serration events, the increase in the GUMs population together with a decrease in FI population resulted in an increase in the number of serration events. Also, it was energetically favourable to re-activate an existing shear band rather than to nucleate a new one. At increased strain magnitudes, it was more probable that slipping took place in an existing shear band leading to more localization of strain, which is a reason for the increase in mean stress drop per event ($\Delta\overline{\sigma}$).

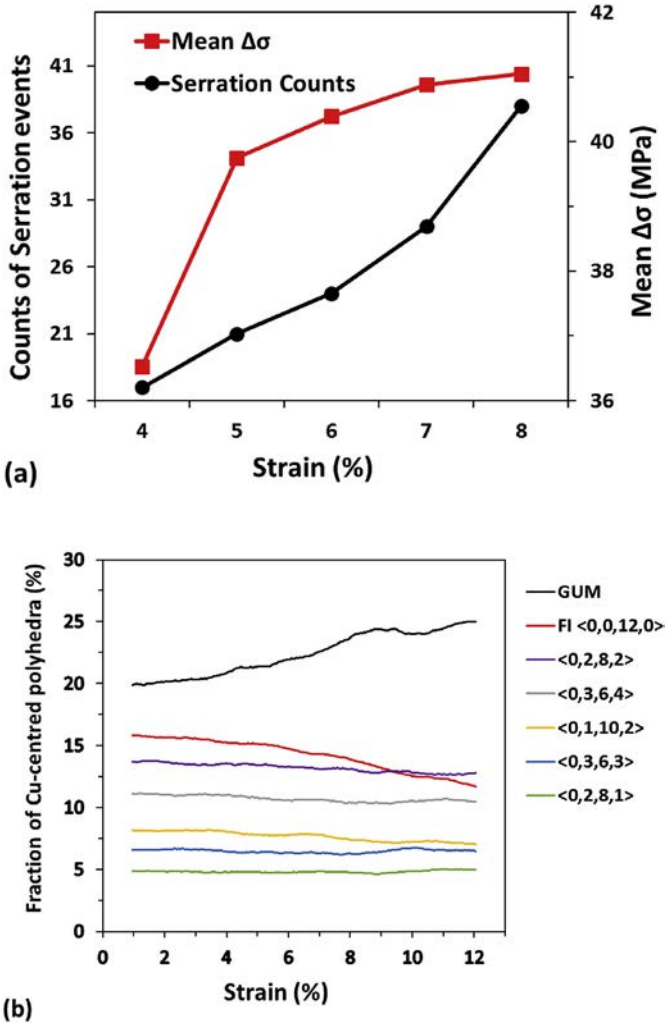

Fig. 8. The evolution of local structure with applied strain. (a) The statistics of serration events with respect to overall sample strain. The number of serration events as well as the mean stress drop per event increase with increase in the overall sample strain. (b) Evolution of six major Cu-centred Voronoi polyhedra and geometrically unfavoured motifs (GUMs) during deformation of the $Cu_{64}Zr_{36}$ MG sample.

3.3. Effect of operating temperature

For studying the effect of temperature on the serration behaviour, uniaxial deformation simulations were carried out on a $Cu_{64}Zr_{36}$ sample over the temperature range from 25 K to 500 K. The resultant stress-strain responses are presented in Fig. 9(a), which shows that the number of serration events consistently increased with increasing temperature. This can be further quantified by calculating the number of serration events and the mean and standard deviation of the amplitude of stress changes at each temperature, as depicted in Fig. 9(b)–(c). Again, to exclude ensemble average effects, only events with $\Delta\sigma > 15$ MPa were considered in the analysis. From Fig. 9(b)–(c), a clear trend of an increase in the number of serration events as well as an increase in the mean and standard deviation of the $\Delta\sigma$ with increasing temperature is evident.

We tracked the decay of FI motifs and the growth of GUMs in the sample with increasing strain as a function of temperature. Fig. 10(a) represents the decay in the population of FI motifs. The population of FI decreased with an increase in temperature. In contrast, the population of GUMs, nucleation sites of STZs, increased with an increase in temperature as depicted in Fig. 10(b). Thus, the decrease in FI population coupled with an increase in the GUMs population resulted in enhanced serration behaviour at higher temperatures.

This agrees with the experimental findings that serration events and serration amplitude decreased with decreasing temperature, and that there was a clear transition from serrated to non-serrated flow at a particular transition temperature T_T [23,33,52]. The transition temperature is dependent on both the applied strain rate and composition of the sample. It is well known that shear transformations (STs) are thermally activated processes. At any strain rate higher temperatures mean more thermal energy is present in the system. This additional thermal energy adds to stress supplied from loading produced more STZs in the sample. These STZs coalesce and participate in slip avalanches leading to enhanced serrated flow. Hence, we observed more serration events with an increased amplitude of $\Delta\sigma$. Also, at higher temperatures, the system has higher entropy and more randomness, which explains the increase in standard deviation of $\Delta\sigma$, as the fluctuation in the amplitude of $\Delta\sigma$ increased due to increased system randomness.

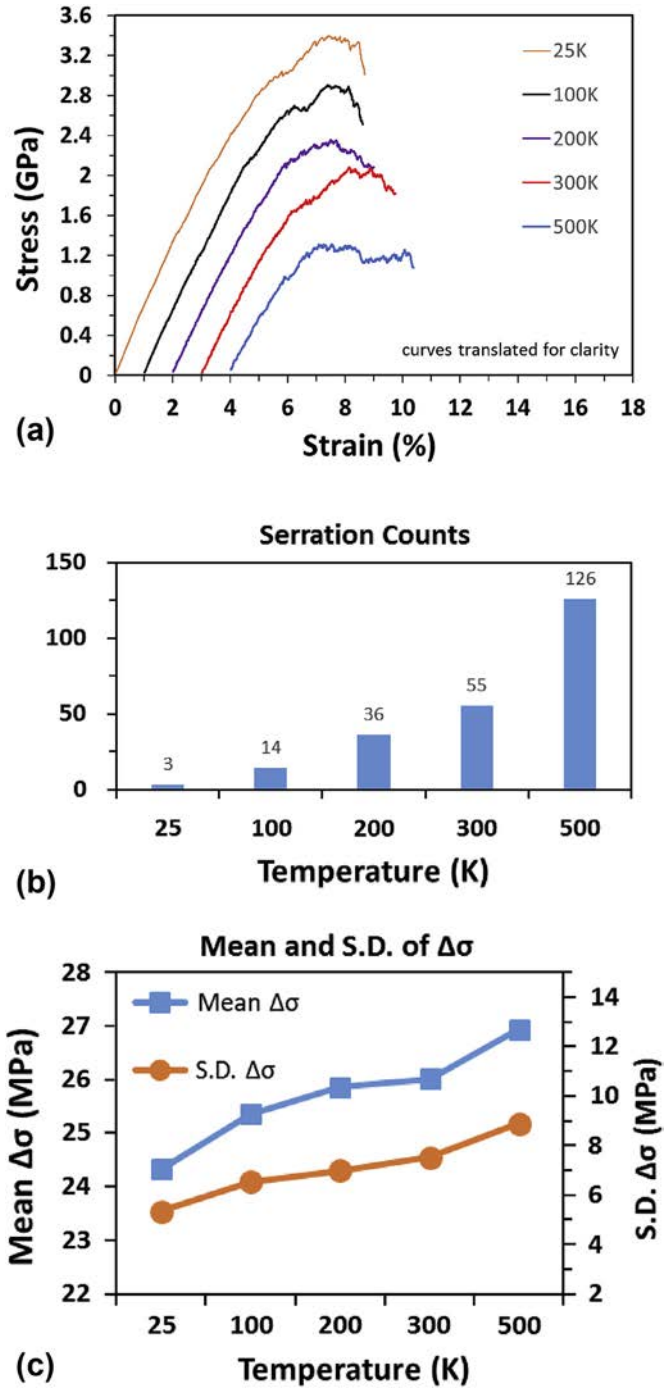

Fig. 9. Effects of temperature. (a) Stress-strain response of the $Cu_{64}Zr_{36}$ MG sample at 10^7 s^{-1} strain rate and varied temperatures. The curves become more and more serrated with increase in temperature, and the maximum strain decreases with increasing temperature. Note the curves are offset from one another for clarity. (b) Evolution of counts of serration events during the deformation of the $Cu_{64}Zr_{36}$ MG sample at varied temperatures. (c) Evolution of mean and standard deviation of magnitude of stress change at different temperatures.

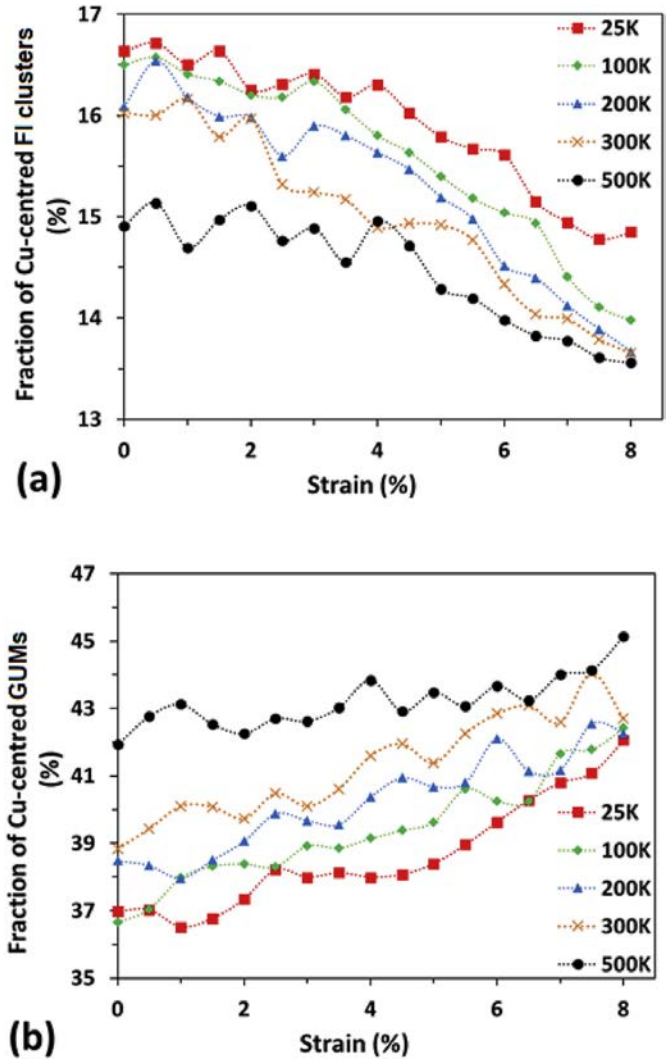

Fig. 10. Voronoi polyhedral type trends with strain. (a) Decay of the population of full icosahedra (FI) clusters during the deformation of the $Cu_{64}Zr_{36}$ MG sample at varied temperatures. The population of FI motifs is lower at higher temperature. (b) Growth of the population of geometrically unfavoured motifs (GUMs) during the deformation of the $Cu_{64}Zr_{36}$ MG sample at varied temperatures. The population of GUMs is higher at higher temperature.

3.4. Effect of strain rate

Uniaxial tensile deformation tests were performed on a $Cu_{64}Zr_{36}$ sample at room temperature (300 K) and varied strain rates ranging from 10^9 $s^{-1} - 5 \times 10^6$ s^{-1}, for investigating the effect of strain rate on serration events. The resultant stress-strain responses are presented in Fig. 11(a). As seen in Fig. 11(a) the plastic deformation became more serrated as the applied strain rate was decreased. This can be quantified by a plot of the mean magnitude of stress drop with respect to the log of strain rate as shown in Fig. 11(b). The mean $\Delta\sigma$ increased linearly with a logarithmic strain rate following the model reported recently by Li et al. based on experimental observations [34].

$$\overline{\Delta\sigma} = A - B\,log(\dot{\varepsilon}) \quad (2)$$

The calculated value of B = 11.09 agreed well with the experimentally reported value of B = 10.5. The accuracy of our fit is $R^2 = 0.97$.

This trend also agreed very well with experimental observations by Antonaglia et al. and Dalla Torre et al. where similar trends were observed [32,52]. Decreasing the strain rate slows the system dynamics, which in turn provided more time for the atoms in the sample to move inelastically allowing more structural dilation. Structural breakdown resulted in an increase in the population of GUMs and a concomitant decrease in shear resistant FIs, thus

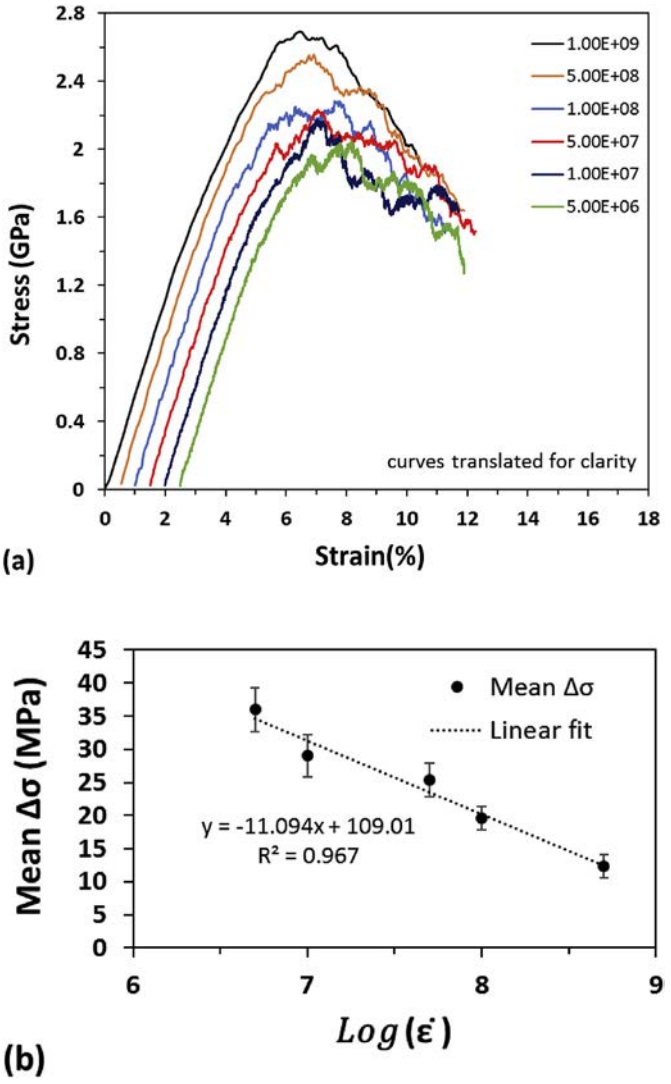

Fig. 11. Strain rate effects. (a) Stress-strain response of the $Cu_{64}Zr_{36}$ MG sample at 300 K and variable strain rate rates. The maximum strength of the sample decreases with a decrease in strain rate. Also, the curves become more and more serrated with a decrease in strain rate. (b) Variation of mean Δσ with respect to strain rate. Five separate simulations were performed at each strain rate to capture the stochasticity by varying the random velocity seed.

leading to an increase in serration events. The slow system dynamics also allow shear bands to propagate for a longer duration before they are arrested, which increases localization into one shear band and is reflected in the increase in amplitude of Δσ.

When the change in temperature is coupled with a change in strain rate, the flow behaviour can be explained based on the atomistic phenomena of thermal activation of STZs and structural dilation in the sample [23,33]. At low strain rates, the athermal driving stress is low. However, slower dynamics allowmore time for structural dilation to take place. Moreover, an increase in temperature increases the thermal activation of STZs. Hence, low applied strain rates and high temperatures favour thermal activation of shear bands and breakdown of the structure into GUMs leading to highly serrated flow. In contrast, a high applied strain rate quickens the system dynamics, thereby not allowing time for structural dilation to take place. Also, at low temperatures there is little thermal activation. Thus, low temperatures and high strain rates favour non-serrated flow.

3.5. Compositional dependence of serration behaviour

$Cu_{64}Zr_{36}$ is known to have one of the best glass-forming abilities amongst Cu-Zr bulk metallic glass compositions and is structurally amongst the most stable. $Cu_{50}Zr_{50}$ and $Cu_{56}Zr_{44}$ are also good glass formers with moderate structural stability while $Cu_{33}Zr_{67}$ is a poor glass former and has the least structural stability. This is reflected in their critical casting diameters: $Cu_{64}Zr_{36}$ (2 mm) [54]; $Cu_{50}Zr_{50}$ (1.1 mm) [55]; $Cu_{56}Zr_{44}$ (1.0 mm) [55] and $Cu_{33}Zr_{67}$ (0.6 mm) [56]. In order to cover the spectrum of Cu-Zr compositions, these four representatives were chosen for analysis.

Fig. 12(a) represents the uniaxial tensile deformation response of the four Cu-Zr compositions at room temperature (300 K). As expected, $Cu_{64}Zr_{36}$ has the highest strength and Young's modulus amongst all compositions. The strength and Young's modulus showed a declining trend with decreasing Cu content. The serration behaviour follows the same trend as the stress-strain curves appeared more and more serrated with decreasing Cu content. A statistical analysis was performed to calculate counts of serration events and the mean and standard deviation of the amplitude of stress change is shown in Fig. 12(b)–(c). It is evident that both the number of serration events and the magnitude and standard deviation of the amplitude of stress change showed an increasing trend with decreasing Cu content.

Fig. 12(d) represents the frequency of full icosahedral (FI) and geometrically unfavoured motifs (GUMs) in the undeformed samples for the four Cu-Zr compositions under study. It is clear from the figure that the population of FI motifs increased with increasing Cu content whereas the population of GUMs decreased with increasing Cu content. Thus, $Cu_{64}Zr_{36}$ had the highest population of shear-resistant FI motifs, whereas $Cu_{50}Zr_{50}$ and $Cu_{56}Zr_{44}$ have a lesser population of FI motifs, and $Cu_{35}Zr_{65}$ has the least of all. The population of GUMs followed the inverse trend. As discussed earlier, FI motifs are most resistant to shear transformations and they form the structural backbone of the glass. Plastic deformation took place only when the strong fabric of FI's were broken, eventually evolving into GUMs. These GUMs acted as sites of STZ nucleation giving rise to serrated flow. This explains very well the current trends in serration behaviour of different Cu-Zr compositions analysed here. Hence, the $Cu_{35}Zr_{65}$ sample exhibited greater serrated flow compared to $Cu_{50}Zr_{50}$ or $Cu_{56}Zr_{44}$, and $Cu_{64}Zr_{36}$ exhibited the least serrated flow. This also agrees with experimental observations by Lee et al. [53] as they found that the plasticity decreased with increasing Cu content from $Cu_{50}Zr_{50}$ to $Cu_{65}Zr_{35}$.

4. Conclusions

In summary, MD was used to prepare MG samples with Cu_xZr_{100-x} (x = 35, 50, 56 and 64) compositions by a relax-melt-quench procedure and used to simulate uniaxial tensile deformation. Stress-strain curves with profuse, discernible serration events were obtained.

The underlying short-range structural origins of serration events were revealed. The analysis showed that stress drop events occurred due to coupled slipping of several atoms present in specific groups/clusters. By one to one mapping of these atoms to their corresponding Voronoi polyhedra we found that most of these groups belonged to the class of geometrically unfavoured motifs acting as 'weak spots' in the amorphous matrix. In contrast, the stress accumulation events showed little plastic deformation as no new shear transformation zones were visible in the sample as the system moved from a low stress state to a high stress state. There was an increase in the number and magnitude of stress drop events during the late stages of deformation due to the breakdown and

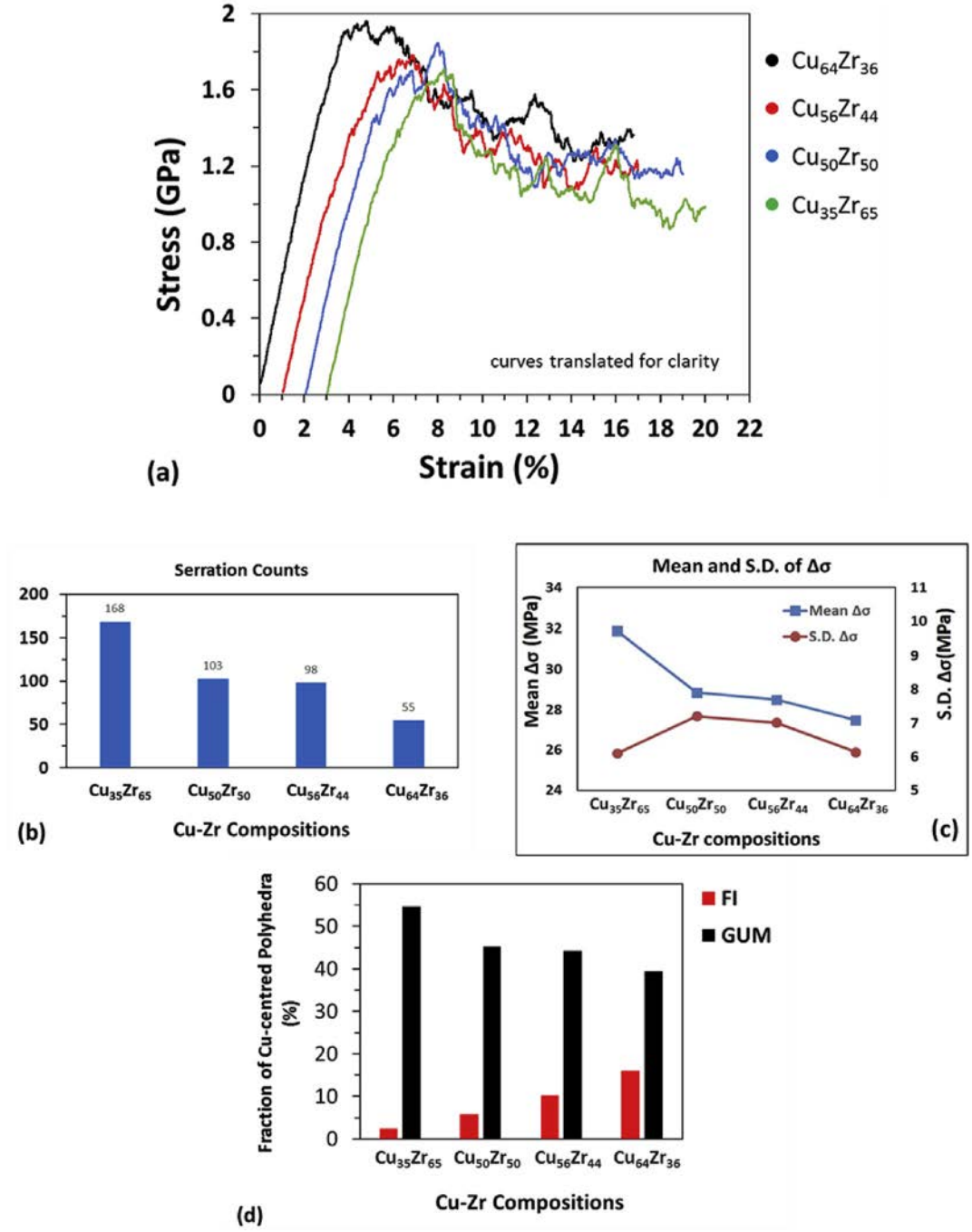

Fig. 12. Effects of Cu:Zr composition. (a) Stress-strain response of four different compositions of Cu-Zr MG at 300 K and 10^7 s^{-1} strain rate. The $Cu_{64}Zr_{36}$ sample has the greatest maximum strength and highest Young's modulus among all compositions. (b) Trend of counts of serration events in different Cu-Zr compositions. (c) Trend of mean and standard deviation of magnitude of stress change in different Cu-Zr compositions. (d) The population of geometrically unfavoured motifs (GUMs) and full icosahedra (FI) clusters in the undeformed samples of various Cu-Zr compositions. The fraction of FI motifs increases whereas the fraction of GUMs decreases with increasing Cu content. A high fraction of GUMs together with a low fraction of FI motifs leads to enhanced serration behaviour.

evolution of full icosahedral motifs into GUMs.

The effects of different testable parameters were studied. The serration behaviour was found to become more prominent with increasing operating temperature due to the increase in GUM population, nucleation sites for STZs, together with a decrease in shear resistant FI motifs. Slower system dynamics at low strain rates tended to allow more time for atoms to participate in coupled slipping, thereby giving rise to enhanced serration behaviour at lower strain rates. A linear relationship between the mean stress drop of serration events and the logarithm of strain rate was observed. Finally, the trend of a decrease in the FI population and increase in the GUMs population with decreasing Cu content in the Cu-Zr MG compositions was shown to correspond with serration behaviour becoming more prominent in low Cu content compositions.

The observations obtained from this analysis have a broader

applicability for understanding the atomistic origins of serration behaviour and the effect of operating parameters on the serrated flow of metallic glasses.

Declarations of interest

None.

Acknowledgements

The authors acknowledge the financial support provided by the Natural Sciences and Engineering Research Council of Canada (NSERC) and Gedex Inc. Computations were performed on the GPC supercomputer at the SciNet HPC Consortium [57]. SciNet is funded by the Canada Foundation for Innovation under the auspices of Compute Canada; the Government of Ontario; Ontario Research Fund - Research Excellence; and the University of Toronto.

References

[1] W.L. Johnson, Bulk glass-forming metallic alloys: science and technology, MRS Bull. 24 (1999) 42–56.
[2] J.F. Löffler, Bulk metallic glasses, Intermetallics 11 (2003) 529–540.
[3] M. Telford, The case for bulk metallic glass, Mater. Today 7 (2004) 36–43.
[4] C. Schuh, T. Hufnagel, U. Ramamurty, Mechanical behavior of amorphous alloys, Acta Mater. 55 (2007) 4067–4109.
[5] M.M. Trexler, N.N. Thadhani, Mechanical properties of bulk metallic glasses, Prog. Mater. Sci. 55 (2010) 759–839.
[6] A. Lund, C. Schuh, The Mohr–Coulomb criterion from unit shear processes in metallic glass, Intermetallics 12 (2004) 1159–1165.
[7] S. Scudino, Mechanism of shear banding during cold rolling of a bulk metallic glass, J. Alloy. Comp. 773 (2019) 883–889.
[8] D.G. Dunaev, A.T. Kosilov, A.V. Evteev, E.V. Levchenko, Structure change of the $Cu_{64}Zr_{36}$ metallic glass in the conditions of uniaxial deformation, Glass Phys. Chem. 39 (2013) 155–161.
[9] J.E. Velasco, A. Concustell, E. Pineda, D. Crespo, Plastic deformation induced anisotropy in metallic glasses: a molecular dynamics study, J. Alloy. Comp. 707 (2017) 102–107.
[10] A. Lagogianni, G. Almyras, C. Lekka, D. Papageorgiou, G. Evangelakis, Structural characteristics of Cu_xZr_{100-x} metallic glasses by molecular dynamics simulations, J. Alloy. Comp. 483 (2009) 658–661.
[11] L. Ward, S.C. O'Keeffe, J. Stevick, G.R. Jelbert, M. Aykol, C. Wolverton, A machine learning approach for engineering bulk metallic glass alloys, Acta Mater. 159 (2018) 102–111.
[12] C. Lekka, Cu–Zr and Cu–Zr–Al clusters: bonding characteristics and mechanical properties, J. Alloy. Comp. 504 (2010) S190–S193.
[13] C. Fan, A. Inoue, Ductility of bulk nanocrystalline composites and metallic glasses at room temperature, Appl. Phys. Lett. 77 (2000) 46–48.
[14] Y.H. Liu, G. Wang, R.J. Wang, D.Q. Zhao, M.X. Pan, W.H. Wang, Super plastic bulk metallic glasses at room temperature, Science 315 (2007) 1385–1388.
[15] H. Li, P.K. Liaw, H. Choo, On the serrated behavior during plastic deformation of a Zr-based bulk metallic glass, Mater. Trans. 48 (2007) 2919–2922.
[16] Y. Zhang, W.H. Wang, A.L. Greer, Making metallic glasses plastic by control of residual stress, Nat. Mater. 5 (2006) 857–860.
[17] C. Meduri, M. Hasan, S. Adam, G. Kumar, Effect of temperature on shear bands and bending plasticity of metallic glasses, J. Alloy. Comp. 732 (2018) 922–927.
[18] A. Argon, Plastic deformation in metallic glasses, Acta Metall. Mater. 27 (1979) 47–58.
[19] J. Pan, Y.X. Wang, Q. Guo, D. Zhang, A.L. Greer, Y. Li, Extreme rejuvenation and softening in a bulk metallic glass, Nat. Commun. 9 (2018), https://doi.org/10.1038/s41467-018-02943-4.
[20] A. Dubach, F.H. Dalla Torre, J. Loffler, Constitutive model for inhomogeneous flow in bulk metallic glasses, Acta Mater. 57 (2009) 881–892.
[21] B.A. Sun, S. Pauly, J. Hu, W.H. Wang, U. Kühn, J. Eckert, Origin of intermittent plastic flow and instability of shear band sliding in bulk metallic glasses, Phys. Rev. Lett. 110 (2013) 225501.
[22] D. Klaumünzer, R. Maaß, J.F. Löffler, Stick-slip dynamics and recent insights into shear banding in metallic glasses, J. Mater. Res. 26 (2011) 1453–1463.
[23] P. Thurnheer, R. Maaß, K. Laws, S. Pogatscher, J. Löffler, Dynamic properties of major shear bands in Zr–Cu–Al bulk metallic glasses, Acta Mater. 96 (2015) 428–436.
[24] C. Pampillo, H. Chen, Comprehensive plastic deformation of a bulk metallic glass, Mater. Sci. Eng. 13 (1974) 181–188.
[25] C.A. Schuh, A.C. Lund, Atomistic basis for the plastic yield criterion of metallic glass, Nat. Mater. 2 (2003) 449–452.
[26] D.B. Miracle, A structural model for metallic glasses, Nat. Mater. 10 (2004) 786–787.
[27] J. Zhou, B. Sun, Q. Wang, Q. Yang, W. Yang, B. Shen, Effects of Ni and Si additions on mechanical properties and serrated flow behavior in FeMoPCB bulk metallic glasses, J. Alloy. Comp. 783 (2019) 555–564.
[28] R. Rashidi, M. Malekan, Y. Hamishebahar, Serration dynamics in the presence of chemical heterogeneities for a Cu-Zr based bulk metallic glass, J. Alloy. Comp. 775 (2019) 298–303.
[29] L.H. Liu, Z.Y. Liu, Y. Huan, X.Y. Wu, Y. Lou, X.S. Huang, L.J. He, P.J. Li, L.C. Zhang, Effect of structural heterogeneity on serrated flow behavior of Zr-based metallic glass, J. Alloy. Comp. 766 (2018) 908–917.
[30] G.K. Liao, Z.L. Long, M.S.Z. Zhao, L. Peng, W. Chai, Z.H. Ping, Nanoindentation study in the characteristic of shear transformation zone in a Pd-based bulk metallic glass during serrated flow, Physica B 534 (2018) 163–168.
[31] J. Antonaglia, W.J. Wright, X. Gu, R.R. Byer, T.C. Hufnagel, M. Leblanc, et al., Bulk metallic glasses deform via slip avalanches, Phys. Rev. Lett. 112 (2014) 155501.
[32] J. Antonaglia, X. Xie, G. Schwarz, M. Wraith, J. Qiao, Y. Zhang, et al., Tuned critical avalanche scaling in bulk metallic glasses, Sci. Rep. 4 (2014), https://doi.org/10.1038/srep04382.
[33] P. Thurnheer, R. Maaß, S. Pogatscher, J.F. Löffler, Compositional dependence of shear-band dynamics in the Zr–Cu–Al bulk metallic glass system, Appl. Phys. Lett. 104 (2014) 101910.
[34] J. Li, Z. Wang, J. Qiao, Power-law scaling between mean stress drops and strain rates in bulk metallic glasses, Mater. Des. 99 (2016) 427–432.
[35] S.D. Feng, K.C. Chan, S.H. Chen, L. Zhao, R.P. Liu, The role of configurational disorder on plastic and dynamic deformation in $Cu_{64}Zr_{36}$ metallic glasses: a molecular dynamics analysis, Sci. Rep. 7 (2017), https://doi.org/10.1038/srep40969.
[36] C. Tang, K. Laws, M. Ferry, Atomistic origin of stress overshoots and serrations in a CuZr metallic glass, Materialia 1 (2018) 121–127.
[37] W. Da, P. Wang, Y. Wang, M. Li, L. Yang, Inhomogeneity of free volumes in metallic glasses under tension, Materials 12 (2019) 98.
[38] S. Plimpton, Fast parallel algorithms for short-range molecular dynamics, J. Comput. Phys. 117 (1995) 1–19.
[39] M. Mendelev, M. Kramer, R. Ott, D. Sordelet, D. Yagodin, P. Popel, Development of suitable interatomic potentials for simulation of liquid and amorphous Cu–Zr alloys, Philos. Mag. A 89 (2009) 967–987.
[40] S. Sedighi, D.W. Kirk, C.V. Singh, S.J. Thorpe, Investigating the atomic level influencing factors of glass forming ability in NiAl and CuZr metallic glasses, J. Chem. Phys. 143 (2015) 114509.
[41] D. Louzguine-Luzgin, V. Zadorozhnyy, N. Chen, S. Ketov, Evidence of the existence of two deformation stages in bulk metallic glasses, J. Non-Cryst. Solids 396–397 (2014) 20–24.
[42] B. Shi, S. Luan, P. Jin, Crossover from free propagation to cooperative motions of shear bands and its effect on serrated flow in metallic glass, J. Non Cryst. Sol. 482 (2018) 126–131.
[43] G. Afonin, S. Khonik, R. Konchakov, N. Kobelev, A. Kaloyan, V. Khonik, Internal stresses induced by plastic shear deformation of Zr–(Cu,Ag)–Al bulk metallic glasses, J. Non-Cryst. Solids 358 (2012) 220–223.
[44] A. Vinogradov, M. Seleznev, I.S. Yasnikov, Dislocation characteristics of shear bands in metallic glasses, Scripta Mater. 130 (2017) 138–142.
[45] N. Mattern, P. Jóvári, I. Kaban, S. Gruner, A. Elsner, V. Kokotin, et al., Short-range order of Cu–Zr metallic glasses, J. Alloy. Comp. 485 (2009) 163–169.
[46] J. Li, AtomEye: an efficient atomistic configuration viewer, Model. Simulat. Mater. Sci. Eng. 11 (2003) 173–177.
[47] A. Stukowski, Visualization and analysis of atomistic simulation data with OVITO–the Open visualization tool, Model. Simulat. Mater. Sci. Eng. 18 (2009), 015012.
[48] F. Shimizu, S. Ogata, J. Li, Theory of shear banding in metallic glasses and molecular dynamics calculations, Mater. Trans. 48 (2007) 2923–2927.
[49] H.W. Sheng, W.K. Luo, F.M. Alamgir, J.M. Bai, E. Ma, Atomic packing and short-to-medium-range order in metallic glasses, Nature 439 (2006) 419–425.
[50] C. Rycroft, Voro++: a three-dimensional Voronoi cell library in C, Chaos 19 (2009), 041111.
[51] J. Ding, S. Patinet, M.L. Falk, Y. Cheng, E. Ma, Soft spots and their structural signature in a metallic glass, Proc. Natl. Acad. Sci. U.S.A. 111 (2014) 14052–14056.
[52] F.H. Dalla Torre, A. Dubach, A. Nelson, J.F. Löffler, Temperature, strain and strain rate dependence of serrated flow in bulk metallic glasses, Mater. Trans. 48 (2007) 1774–1780.
[53] J.-C. Lee, K.-W. Park, K.-H. Kim, E. Fleury, B.-J. Lee, M. Wakeda, et al., Origin of the plasticity in bulk amorphous alloys, J. Mater. Res. 22 (2007) 3087–3097.
[54] D. Xu, B. Lohwongwatana, G. Duan, W.L. Johnson, C. Garland, Bulk metallic glass formation in binary Cu-rich alloy series – Cu100–xZrx (x=34, 36, 38.2, 40 at.%) and mechanical properties of bulk Cu64Zr36 glass, Acta Mater. 52 (2004) 2621–2624.
[55] Y. Li, Q. Guo, J.A. Kalb, C.V. Thompson, Matching glass-forming ability with the density of the amorphous phase, Science 322 (2008) 1816–1819.
[56] E. Babić, R. Ristić, I.A. Figueroa, D. Pajić, Ž. Skoko, K. Zadro, Electronic structure and glass forming ability in early and late transition metal alloys, Philos. Mag. A 98 (2017) 693–709.
[57] C. Loken, D. Gruner, L. Groer, R. Peltier, N. Bunn, M. Craig, et al., SciNet: lessons learned from building a power-efficient top-20 system and data centre, J. Phys. Conf. Ser. 256 (2010), 012026.